Dynamical Mean-Field Theory Plus Numerical Renormalization-Group Study of Spin-Orbital Separation in a Three-Band Hund Metal

K. M. Stadler, Z. P. Yin, J. von Delft, G. Kotliar, and A. Weichselbaum

DMFT+NRG study of spin-orbital separation in a three-band Hund's metal

K. M. Stadler,[1] Z. P. Yin,[2] J. von Delft,[1] G. Kotliar,[2] and A. Weichselbaum[1]

[1] *Physics Department, Arnold Sommerfeld Center for Theoretical Physics and Center for NanoScience,*
Ludwig-Maximilians-Universität München, 80333 München, Germany
[2] *Department of Physics and Astronomy, Rutgers University, Piscataway, NJ 08854, USA*
(Dated: submitted April 21 2015; revised July 31 2015)

We show that the numerical renormalization group (NRG) is a viable multi-band impurity solver for Dynamical Mean Field Theory (DMFT), offering unprecedented real-frequency spectral resolution at arbitrarily low energies and temperatures. We use it to obtain a numerically exact DMFT solution to the Hund's metal problem for a three-band model on a Bethe lattice at 1/3 filling. The ground state is a Fermi liquid. The one-particle spectral function undergoes a coherence-incoherence crossover with increasing temperature, with spectral weight being transfered from low to high energies. Further, it exhibits a strong particle-hole asymmetry. In the incoherent regime the self-energy displays approximate power-law behavior for positive frequencies only. The spin and orbital spectral functions show "spin-orbital separation": spin screening occurs at much lower energies than orbital screening. The renormalization group flows clearly reveal the relevant physics at all energy scales.

Introduction.— A widely-used method for dealing with interactions in strongly-correlated electron systems and electronic structure calculations is dynamical mean field theory (DMFT) [1, 2]. It treats the interplay between a given lattice site (the "impurity") and the rest of the lattice (the "bath") as a quantum impurity model with a self-consistently determined hybridization function. Since DMFT's performance depends on that of the method used to solve this impurity model, much effort has been invested over the years to develop ever more powerful impurity solvers. For multi-band models, continuous-time Quantum Monte Carlo (ctQMC) methods appear to be the current favorites in terms of versatility and performance [3]. However, they are not without limitations: sign problems can occur, low-temperature calculations are costly, and obtaining real-frequency spectra requires analytic continuation of imaginary (Matsubara) frequency QMC data, which is notoriously difficult. Thus, there is a continued need for *real-frequency* impurity solvers suitable for *multi-band* DMFT applications.

In this work, we show that the numerical renormalization group (NRG) [4–6] is such a tool, offering unprecedented real-frequency spectral resolution at low energies. NRG is the gold standard for impurity models, with numerous previous DMFT applications (e.g. [7–13]), but so far was limited to models with at most two bands. However, recent technical progress [14–16] has now made three-band calculations feasible [17–19].

We illustrate the potential of DMFT+NRG by studying the minimal model [20–22] of a three-band "Hund's metal" [23, 24], which has both a Hubbard interaction U and a ferromagnetic Hund's coupling J, with $U(1)_{ch} \times SU(2)_{sp} \times SU(3)_{orb}$ symmetry for its charge (ch), spin (sp) and orbital (orb) degrees of freedom. Hund's metals are multi-orbital materials with broad bands which are correlated via the Hund-J rather than the Hubbard-U interaction. Examples are iron pnictide and chalcogenide high-temperature superconductors [23, 25], ruthen-

ates [26, 27], and other 4d transition metal oxides [21, 28].

Early DMFT studies using continuous-time QMC (ctQMC) [3] as impurity solver suggest that consequences of the Hund's rule coupling include (i) Fermi-liquid behavior at low energies [23] and (ii) a coherence-incoherence crossover with increasing temperature [23], relevant for various material systems [27, 29]. The incoherent regime is characterized by (iii) a fractional power law for the imaginary part of the Matsubara self-energy [20, 26, 30] and (iv) the coexistence of fast quantum mechanical orbital fluctuations and slow spin fluctuations [20]. However, since ctQMC can not reach truly low temperatures, (i) could not be conclusively established yet, and a more detailed understanding of (ii-iv) is difficult to achieve based on imaginary-frequency data alone. Our real-frequency DMFT+NRG results definitively settle these issues and yield further insights. For the parameters used in our study, we find (i) a Fermi liquid ground state; a real-frequency one-particle spectral function showing (ii) a coherence-incoherence crossover (driven by Hund-J, not Hubbard-U) with significant transfer of spectral weight from low to high energies, and (iii) strong particle-hole asymmetry, which leads to the above-mentioned apparent fractional power laws; (iv) two-stage screening, where spin screening occurs at much lower energies than orbital screening ("spin-orbital separation"); (v) and $T = 0$ spectral properties that are similar with or without DMFT self-consistency, in contrast to Mott-Hubbard systems, where the DMFT self-consistency opens a gap in the quasiparticle spectrum at large interaction strength.

Model:— Our three-band model has the Hamiltonian

$$\hat{H} = \sum_i \left(-\mu \hat{N}_i + \hat{H}_{\text{int}}[\hat{d}_{i\nu}^\dagger] \right) + \sum_{\langle ij \rangle \nu} t\, \hat{d}_{i\nu}^\dagger \hat{d}_{j\nu}, \quad \text{(1a)}$$

$$\hat{H}_{\text{int}}[\hat{d}_{i\nu}^\dagger] = \tfrac{3}{4}J\hat{N}_i + \tfrac{1}{2}\left(U - \tfrac{1}{2}J\right)\hat{N}_i(\hat{N}_i - 1) - J\hat{\mathbf{S}}_i^2. \quad \text{(1b)}$$

Here $\hat{d}_{i\nu}^\dagger$ creates an electron on site i of flavor (fl) ν, with composite index $\nu = (m\sigma)$ labelling its spin ($\sigma = \uparrow, \downarrow$)

and orbital ($m = 1, 2, 3$). $\hat{N}_i = \sum_\nu \hat{d}^\dagger_{i\nu} \hat{d}_{i\nu}$ is the total number operator for site i and $\hat{\mathbf{S}}_i$ its total spin, with components $\hat{S}^\alpha_i = \sum_{m\sigma\sigma'} \hat{d}^\dagger_{im\sigma} \frac{1}{2} \sigma^\alpha_{\sigma\sigma'} \hat{d}_{im\sigma'}$, where σ^α are Pauli matrices. We study a Bethe lattice with nearest-neighbor hopping amplitude t, used as energy unit ($t = 1$). Onsite interactions are described by $\hat{H}_{\mathrm{int}}$. The onsite Coulomb interaction U penalizes double occupancy. The ferromagnetic coupling $J > 0$ accounts for Hund's first rule by favoring a large spin per site. We choose the chemical potential μ such that the filling per lattice site is one below half-filling, $\langle \hat{N}_i \rangle \simeq 2$, inducive to an intricate interplay of spin and orbital degrees of freedom.

Methods.— We use single-site DMFT to map the lattice model onto a three-band Anderson-Hund model (AHM) of the form $\hat{H}_{\mathrm{AHM}} = \varepsilon_d \hat{N} + \hat{H}_{\mathrm{int}}[\hat{d}^\dagger_\nu] + \hat{H}_{\mathrm{bath+hyb}}$. Here $d^\dagger_\nu$ creates a local ("impurity") electron of flavor ν with energy $\varepsilon_d = -\mu$, experiencing local interactions $\hat{H}_{\mathrm{int}}$, with total number and spin operators $\hat{N}$ and $\hat{\mathbf{S}}$ defined analogously to $\hat{N}_i$ and $\hat{\mathbf{S}}_i$. The local site on average hosts two electrons ($n_d = \langle \hat{N} \rangle \simeq 2$), forming a spin triplet and orbital triplet (the one hole relative to half-filling can be in one of three orbital levels). The local electrons hybridize with a three-band spinful bath,

$$H_{\mathrm{bath+hyb}} = \sum_{k\nu} \left(\varepsilon_k c^\dagger_{k\nu} \hat{c}_{k\nu} + V_k \left[\hat{d}^\dagger_\nu \hat{c}_{k\nu} + \hat{c}^\dagger_{k\nu} \hat{d}_\nu \right] \right), \quad (2)$$

with a hybridization function $\Gamma(\varepsilon) = \pi \sum_k |V_k|^2 \delta(\varepsilon - \varepsilon_k)$ that fully characterizes the impurity-bath interplay. In DMFT, $\Gamma(\varepsilon)$ has the role of the effective Weiss mean field and is determined self-consistently [1, 2, 31]. We studied both the self-consistent AHM (scAHM), and for comparison also the pure impurity AHM (iAHM) without self-consistency, using a flat density of states with half-bandwidth D, $\Gamma(\varepsilon) \equiv \Gamma \Theta(D - |\varepsilon|)$.

We use full-density-matrix (fdm) NRG [32] exploiting non-Abelian symmetries [15], both to solve the iAHM and for each scAHM iteration (for NRG details, see [31]). The key idea of NRG, due to Wilson [4], is to discretize the bath's continuous spectrum logarithmically, map the model onto a semi-infinite "Wilson" chain with exponentially decaying hopping amplitudes, and exploit this energy-scale separation to iteratively diagonalize the model while discarding high-energy states. This allows one to zoom in on low-energy properties, at the expense of having only coarse-grained resolution at high energies. Nevertheless, NRG results are accurate also for spectral integrals even if these include large energies, since they can be evaluated using discrete, unbroadened NRG data.

Matsubara benchmark.— We illustrate this by benchmarking NRG versus ctQMC [31], which treats the bath as a continuum and has no bath discretization issues. We used both methods to compute the self-energy $\Sigma(i\omega_n)$ of the Matsubara correlator $G(i\omega_n)$ associated with the retarded local correlator $G^R(\omega) = \langle d_\nu \| d^\dagger_\nu \rangle_\omega$. In NRG, its spectral function is expressed in terms of discrete data, $A(\omega) = -\frac{1}{\pi} \mathrm{Im}\, G^R(\omega) \overset{\mathrm{NRG}}{\simeq} \sum_s a_s \delta(\omega - \xi_s)$, hence $G(i\omega_n) =$
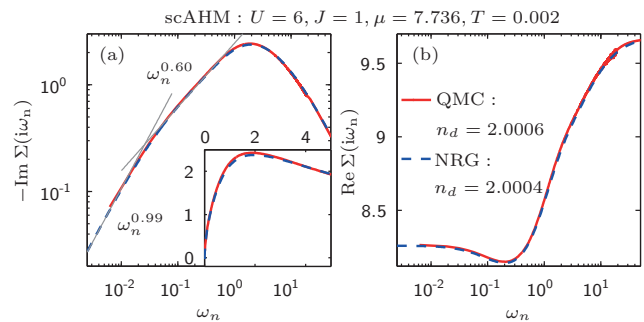

Figure 1. (Color online) Benchmark comparison of NRG and ctQMC for the three-band scAHM. (a) Imaginary and (b) real part of the self-consistently converged self-energy as function of Matsubara frequencies. Grey lines in (a) are power-law fits to low and intermediate frequency data, respectively. The inset of (a) shows $\mathrm{Im}\,\Sigma(i\omega_n)$ on a linear scale.

$\int d\omega A(\omega)/(i\omega_n - \omega) \overset{\mathrm{NRG}}{\simeq} \sum_s a_s/(i\omega_n - \xi_s)$. Fig. 1 compares NRG and ctQMC results for $\Sigma(i\omega_n)$ at $T = 0.002$. The agreement is excellent, also at large frequencies [with relative deviations of $\lesssim 2.5\%$ for $\mathrm{Im}\Sigma(i\omega_n)$ and $\lesssim 0.5\%$ for $\mathrm{Re}\Sigma(i\omega_n)$]. However, the numerical costs differ vastly ($\simeq 10^2$ vs. 10^4 CPU hours) [31], since the chosen temperature is challengingly low for ctQMC, whereas NRG can access any temperature. Luttinger pinning at zero frequency [1, 33] is fulfilled within 1% for both methods [31]. $\mathrm{Im}\,\Sigma(i\omega_n)$ displays fractional power-law behavior for intermediate frequencies ($0.05 \lesssim \omega_n \lesssim 0.5$), as found in [20, 26], and Fermi-liquid behavior ($\propto \omega_n$) for very low frequencies, as found in [23, 27], but not in [26].

Coherence-incoherence crossover. We now turn to real-frequency properties [Fig. 2]. At zero temperature, the local spectral function $A(\omega)$ of the scAHM shows a well-defined low-energy quasiparticle peak and $-\mathrm{Im}\,\Sigma^R(\omega)$ a dip reaching down to zero [insets of Figs. 2(a,b)]. This indicates that strong Kondo-type screening correlations exist between bath and local spin and orbital degrees of freedom. At higher energies, $A(\omega)$ also shows incoherent, rather flat particle-hole asymmetric side peaks, that reflect charge fluctuation.

With increasing temperature, a coherence-incoherence crossover occurs: the quasiparticle peak first weakens and then gives way to a pseudogap [Fig. 2(a)]; concurrently the dip in $-\mathrm{Im}\,\Sigma^R(\omega)$ is first smeared out into a broader minimum, which then changes into a maximum [Fig. 2(b)]. During this process, quasiparticle weight is transferred from low to high energies, in a way reminiscent of recent photoemission measurements [34–36] (see Fig. S-4 in [31]). Note that the spectral weight near $\omega \simeq 0$ remains nonzero at all temperatures, implying that metallic behavior persists for the parameters studied here. The evolution of these features to those of the Mott transition that occurs for larger values of U is left for future investigation.

Since the scAHM is based on an impurity model, it is instructive to study a corresponding iAHM, with parameters tuned to yield a similar spectral function at $T = 0$
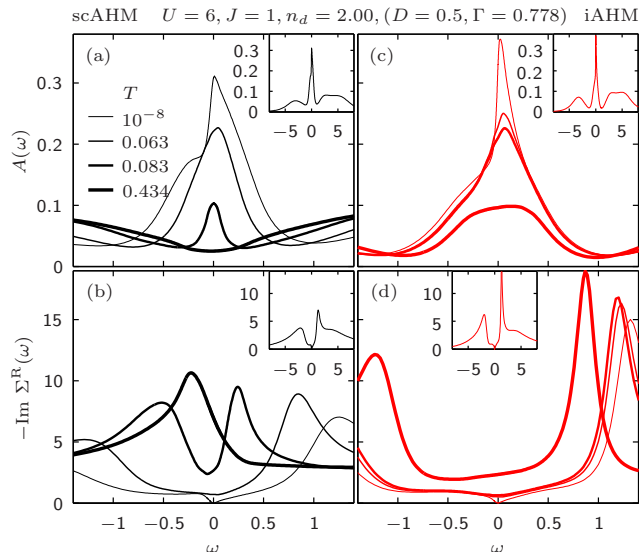
Figure 2. (Color online) (a) The local spectral function $A(\omega)$ and (b) the imaginary part of the retarded self-energy, $\mathrm{Im}\,\Sigma^R(\omega)$, for the scAHM, plotted versus frequency for four temperatures. Insets show a larger frequency range for $T = 10^{-8}$. (c,d) Same as in (a,b), but for an iAHM.

[Fig. 2(c,d)]. It likewise features a large low-energy (Kondo) peak that weakens with increasing temperature, though no pseudogap occurs. This shows that the $T = 0$ spectral properties of the scAHM are governed by the impurity physics of the iAHM. The transfer of spectral weight with increasing T is driven by Hund-J for both iAHM and scAHM (see Fig. S-2 of [31]), and for the latter it is amplified by DMFT-self-consistency [compare Figs. 2(a,b)].

Particle-hole asymmetry. We next exploit the power of NRG to zoom in to arbitrarily low energy scales: In Figs. 3(a,b), we replot on a logarithmic scale the data (black/red for sc/iAHM) from Figs. 2(a-d) for $A(\omega)$ and $\mathrm{Im}\,\Sigma^R(\omega)$ at $T = 10^{-8}$. For comparison, the right column of Fig. 3 again shows results for the iAHM, but using parameters that yield smaller crossover scales (defined below), to better separate the low-energy features associated with spin and orbital screening from high-energy features associated with charge fluctuations. Note again the striking qualitative similarity between the scAHM (black) and iAHM (red/blue) spectra − clearly, for $T \simeq 0$ DMFT self-consistency plays no major role.

With decreasing temperature, the quasiparticle peaks in Figs. 2(a,c) show an increasing particle-hole asymmetry, not surprising away from half-filling, which at $T \simeq 0$ is very pronounced: in Figs. 3(a,d) for $A(\omega)$, the thick ($\omega < 0$) lines show a shoulder-like structure for intermediate frequencies (between the vertical solid and dashed lines), while the thin ($\omega > 0$) lines do not; and in Figs. 3(b,e) for $\mathrm{Im}\,\Sigma^R(\omega)$, the thick lines show a plateau-like structure, whereas the thin lines show approximate $\sim \omega^\alpha$ power-law behavior (with non-universal α). For the Matsubara self-energy obtained via the Hilbert trans-
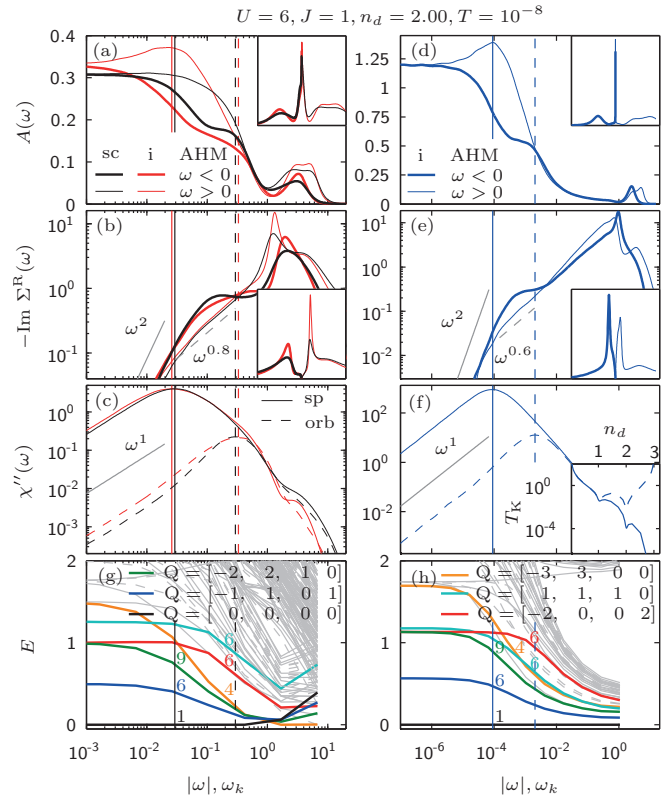

Figure 3. (Color online) (a-f) Spin-orbital separation in real-frequency, ground state correlators. The left column uses the same parameters and color code as Fig. 2 for the scAHM (black) and iAHM with $(\Gamma, D) = (0.778, 0.5)$ (red). For comparison, the right column shows iAHM results with $(\Gamma, D) = (0.200, 1.0)$ (blue), yielding smaller crossover scales. (a,d) The local spectral functions, (b,e) the local self-energy, and (c,f) the spin and orbital susceptibilities, χ''_{sp} (solid) and χ''_{orb} (dashed). We use a logarithmic frequency scale, with thick (thin) lines for $\omega < 0$ ($\omega > 0$). Insets show data on a linear scale. In all panels, solid (dashed) vertical lines mark the spin (orbital) Kondo scale, $T_{\mathrm{K}}^{\mathrm{sp}}$ ($T_{\mathrm{K}}^{\mathrm{orb}}$). Grey guide-to-the eye lines indicate Fermi-liquid power laws (solid) or apparent fractional power laws (dashed). Inset to (f): Kondo scales $T_{\mathrm{K}}^{\mathrm{sp}}$ (solid) and $T_{\mathrm{K}}^{\mathrm{orb}}$ (dashed) for the iAHM, plotted as function of n_d. (g) and (h) show NRG eigenlevel flow diagrams for the scAHM and iAHM of panels (a-c) and (d-f), respectively: the rescaled energies of the lowest-lying eigenmultiplets of a Wilson chain of (even) length k are plotted versus its characteristic level spacing $\omega_k \propto \Lambda^{-k/2}$ (see text). Numbers above lines give multiplet degeneracies, Q their symmetry labels.

form $\Sigma(i\omega_n) = -\frac{1}{\pi}\int d\omega\,\mathrm{Im}\,\Sigma^R(\omega)/(i\omega_n - \omega)$, the asymmetric contributions from the power-law and shoulder in $\mathrm{Im}\,\Sigma^R(\omega \gtrless 0)$ conspire in such a way that $\mathrm{Im}\,\Sigma(i\omega_n)$ shows an apparent fractional power law, but $\mathrm{Re}\,\Sigma(i\omega_n)$ does not [Fig. 1(a,b)]. Conversely, this example ilustrates that care is due when drawing real-frequency conclusions from imaginary-frequency power laws: if one is present only for $\mathrm{Im}\,\Sigma(i\omega_n)$, but not for $\mathrm{Re}\,\Sigma(i\omega_n)$ (as in [20, 26]), then $\mathrm{Im}\,\Sigma^R(\omega)$ need not show pure power-law behavior.

Spin-orbital separation. Next we elucidate the screening of local spin and orbital degrees of freedom by the

bath of conduction electrons. To this end, Figs. 3(c,f) respectively show the imaginary part (χ'') of the dynamical susceptibilities of the spin and orbital operators for the impurity site, $\chi_{\mathrm{sp}} = \frac{1}{3}\sum_\alpha \langle \hat{S}^\alpha \| \hat{S}^\alpha \rangle_\omega$ and $\chi_{\mathrm{orb}} = \frac{1}{8}\sum_a \langle \hat{T}^a \| \hat{T}^a \rangle_\omega$, with orbital operators $\hat{T}^a = \sum_{mm'\sigma} \hat{d}^\dagger_{m\sigma} \frac{1}{2}\tau^a_{mm'} \hat{d}_{m'\sigma}$, where τ^a are the SU(3) Gell-Mann matrices, normalized as $\mathrm{Tr}[\tau^a\tau^b] = 2\delta_{ab}$. Both χ''_{sp} and χ''_{orb} exhibit a peak with (nearly) power-law flanks, characteristic of Kondo screening of the local spin and orbital degrees of freedom. Strikingly, for both scAHM and iAHM the peak for χ''_{sp} occurs at a much lower energy and is much higher than for χ''_{orb}. We take the peak positions to define the spin and orbital Kondo scales, $T_{\mathrm{K}}^{\mathrm{sp}}$ and $T_{\mathrm{K}}^{\mathrm{orb}}$ (vertical solid and dashed lines). $T_{\mathrm{K}}^{\mathrm{sp}}$ acts as the coherence scale below which Fermi-liquid behavior ($\mathrm{Im}\Sigma^R(\omega) \propto \omega^2$, $\chi''_{\mathrm{sp,orb}} \propto \omega$, see Figs. 3(b-f), grey lines) sets in. The SU(2)$_{\mathrm{sp}}$ and SU(3)$_{\mathrm{orb}}$ crossover scales differ strongly, $T_{\mathrm{K}}^{\mathrm{sp}} \ll T_{\mathrm{K}}^{\mathrm{orb}}$, because the Kondo temperature for an SU(N) Kondo model scales as $\ln T_{\mathrm{K}} \sim -1/N$ [37]. This implies two-stage screening, with spin screening occuring at significantly lower energies than orbital screening. This "spin-orbital separation", featuring a very small coherence scale and an intermediate regime with screened orbital degrees of freedom coupled to slowly fluctuating, large spins, was first anticipated in Ref. [37], and more recently discussed qualitatively in Refs. [21, 22]. Its explicit demonstration here is a central result of our work.

The inset of Fig. 3(f) depicts $T_{\mathrm{K}}^{\mathrm{sp}}$ and $T_{\mathrm{K}}^{\mathrm{orb}}$ for the iAHM as function of the filling n_d. For $n_d \simeq 1$, where the bare impurity's ground state has SU(6) symmetry also for $J \neq 0$, $T_{\mathrm{K}}^{\mathrm{sp}} \simeq T_{\mathrm{K}}^{\mathrm{orb}} \simeq T_{\mathrm{K}}^{\mathrm{SU(6)}}$. As n_d increases from 1 to 2, $T_{\mathrm{K}}^{\mathrm{sp}}$ and $T_{\mathrm{K}}^{\mathrm{orb}}$ split apart if $J \neq 0$, indicating that spin-orbital separation sets in. (See also Ref. 31, Fig. S-3.) As n_d continues to increase towards 3, $T_{\mathrm{K}}^{\mathrm{sp}}$ drops below the lowest relevant energy scale and $T_{\mathrm{K}}^{\mathrm{orb}}$ becomes very large ($\gtrsim D$), reflecting the fact that for half-filling the orbitals form an orbital singlet from the outset. In this sense, $n_d \simeq 2$ is special: there conditions are optimal for the Hund coupling to align two spins in different orbitals without forming an orbital singlet.

RG flow. In renormalization group (RG) terms, the two-stage screening discussed above is associated with the RG flow between three fixed points, describing high-, intermediate- and low-energy excitations. Their effective fixed point Hamiltonians have ground state multiplets whose spin×orbital structure is triplet×triplet, triplet×singlet and singlet×singlet, implying an impurity contribution to the ground state entropy of $\ln(9)$, $\ln(3)$ and $\ln(1)$, respectively (see Fig. S-5 in [31]). The RG flow between these fixed points can be visualized via NRG eigenlevel flow diagrams [Fig. 3(g,h)]. Technically, they show how the lowest-lying rescaled eigenlevels of a length-k Wilson chain evolve with k, where "rescaled" means given in units of $\omega_k \propto \Lambda^{-k/2}$ (as defined in [6]), where $\Lambda > 1$ is a discretization parameter [31]. Conceptually,

these levels represent the finite-size spectrum of the impurity+bath put in a spherical box of radius $R_k \propto \Lambda^{k/2}$, centered on the impurity [4, 38]: as k increases, the finite-size level spacing $\omega_k \propto 1/R_k$ decreases exponentially. The corresponding flow of the finite-size spectrum is stationary (k-independent) while ω_k lies within an energy regime governed by one of the fixed points, but changes when ω_k traverses a crossover between two fixed points.

Figs. 3(g,h) show this RG flow for the scAHM and the iAHM, revealing similar behavior for both [39]. We label multiplets by their U(1)$_{\mathrm{ch}}\times$SU(2)$_{\mathrm{sp}}\times$SU(3)$_{\mathrm{orb}}$ symmetry labels, $Q = [q, 2S, q_1q_2]$; here q denotes particle number relative to half-filling, S spin, and (q_1q_2) an SU(3) irrep, identified by a Young diagram with $q_1 + q_2$ (q_2) boxes in its first (second) row. The flow of the lowest-lying levels reveals two crossover scales, $T_{\mathrm{K}}^{\mathrm{orb}}$ and $T_{\mathrm{K}}^{\mathrm{sp}}$ (whose spacing, though, is too small for the level flow in between to become stationary [40]). As ω_k drops below $T_{\mathrm{K}}^{\mathrm{orb}}$, orbital screening sets in, favoring orbital singlets $[(q_1q_2) = (00)]$, hence other multiplets rise in energy. Similarly, as ω_k drops below $T_{\mathrm{K}}^{\mathrm{sp}}$, spin screening sets in, favoring spin singlets and pushing up multiplets with $S \neq 0$. For $\omega_k \ll T_{\mathrm{K}}^{\mathrm{sp}}$, the ground state is a spin and orbital singlet $[Q = (0,0,00)]$. We have checked that its excitation spectrum can be interpreted in terms of non-interacting single-particle excitations, thus confirming its Fermi-liquid nature.

Conclusions. We have demonstrated the potential of DMFT+NRG as real-frequency method to treat multiorbital systems, with no need for analytic continuation. Applied to the simplest model of a three-band Hund's metal, it revealed subtle spectral features which are manifestly different from those of Mott-Hubbard systems, and which can be probed in photoemission and STM spectroscopies.

Our work is a first step towards using LDA+DMFT+NRG to calculate AC and DC transport properties in strongly correlated materials. Such applications will typically involve less orbital symmetries than the model studied here, but could be treated using the recent "interleaved" NRG approach of [16]. The latter yields results of comparable accuracy and efficiency as when symmetries can be exploited [41].

A key advantage of NRG is its ability to iteratively uncover the system's RG flow from high to low energies, revealing the relevant physics at each energy scale. In the context of Mott-Hubbard systems, RG ideas have been very fruitful even in very approximate implementations [42–44]. For the present Hund's metal, the numerically exact RG flow achieved via DMFT+NRG revealed a clear, simple picture of the crossover from the incoherent to the coherent Fermi-liquid regime: two-stage screening of first orbital, then spin degrees of freedom. Using DMFT+NRG to gain this type of RG understanding of real material properties would be a worthwhile goal for future research.

––––––––––

[1] A. Georges, G. Kotliar, W. Krauth, and M. J. Rozenberg, Rev. Mod. Phys. 68, 13 (1996).

[2] G. Kotliar, S. Y. Savrasov, K. Haule, V. S. Oudovenko, O. Parcollet, and C. A. Marianetti, Rev. Mod. Phys. 78, 865 (2006).

[3] E. Gull, A. J. Millis, A. I. Lichtenstein, A. N. Rubtsov, M. Troyer, and P. Werner, Rev. Mod. Phys. 83, 349 (2011).

[4] K. G. Wilson, Rev. Mod. Phys. 47, 773 (1975).

[5] R. Bulla, T. A. Costi, and T. Pruschke, Reviews of Modern Physics 80, 395 (2008).

[6] A. Weichselbaum, Phys. Rev. B 86, 245124 (2012).

[7] O. Sakai and Y. Kuramoto, Solid State Commun. 89, 307311 (1994).

[8] R. Bulla, A. C. Hewson, and T. Pruschke, J. Phys.: Condens. Matter 10, 8365 (1998).

[9] R. Bulla, Phys. Rev. Lett. 83, 136 (1999).

[10] R. Bulla, T. A. Costi, and D. Vollhardt, Phys. Rev. B 64, 045103 (2001).

[11] T. Pruschke and R. Bulla, Eur. Phys. J. B 44, 217 (2005).

[12] X. Deng, J. Mravlje, R. Žitko, M. Ferrero, G. Kotliar, and A. Georges, Phys. Rev. Lett. 110, 086401 (2013).

[13] i. c. v. Osolin, T. Pruschke, and R. Žitko, Phys. Rev. B 91, 075105 (2015).

[14] A. I. Tóth, C. P. Moca, O. Legeza, and G. Zaránd, Phys. Rev. B 78, 245109 (2008), arXiv:0802.4332.

[15] A. Weichselbaum, Annals of Physics 327, 2972 (2012).

[16] A. K. Mitchell, M. R. Galpin, S. Wilson-Fletcher, D. E. Logan, and R. Bulla, Phys. Rev. B 89, 121105 (2014).

[17] C. P. Moca, A. Alex, J. von Delft, and G. Zaránd, Phys. Rev. B 86, 195128 (2012).

[18] M. Hanl, A. Weichselbaum, T. A. Costi, F. Mallet, L. Saminadayar, C. Bäuerle, and J. von Delft, Phys. Rev. B 88, 075146 (2013).

[19] M. Hanl, A. Weichselbaum, J. von Delft, and M. Kiselev, Phys. Rev. B 89, 195131 (2014).

[20] Z. P. Yin, K. Haule, and G. Kotliar, Phys. Rev. B 86, 195141 (2012).

[21] A. Georges, L. d. Medici, and J. Mravlje, Annual Rev. of Cond. Mat. Phys. 4, 137 (2013).

[22] C. Aron and G. Kotliar, Phys. Rev. B 91, 041110 (2015).

[23] K. Haule and G. Kotliar, New J. Phys. 11, 025021 (2009).

[24] Z. P. Yin, K. Haule, and G. Kotliar, Nature Mat. 10, 932 (2011).

[25] Z. P. Yin, K. Haule, and G. Kotliar, Nature Physics 7, 294 297 (2011).

[26] P. Werner, E. Gull, M. Troyer, and A. J. Millis, Phys. Rev. Lett 101, 166405 (2008).

[27] J. Mravlje, M. Aichhorn, T. Miyake, K. Haule, G. Kotliar, and A. Georges, Phys. Rev. Lett. 106, 096401 (2011).

[28] L. de Medici, J. Mravlje, and A. Georges, Phys. Rev. Lett. 107, 256401 (2011).

[29] F. Hardy, A. E. Boehmer, D. Aoki, P. Burger, T. Wolf, P. Schweiss, R. Heid, P. Adelmann, Y. X. Yao, G. Kotliar, J. Schmalian, and C. Meingast, Phys. Rev. Lett. 111, 027002 (2013).

[30] S. Akhanjee and A. Tsvelik, Phys. Rev. B 87, 195137 (2013).

[31] See Supplementary Material [url], which includes Refs. [45–47, 49–53] .

[32] A. Weichselbaum and J. von Delft, Phys. Rev. Lett. 99, 076402 (2007).

[33] E. Müller-Hartmann, Z. Phys. B 76, 211 (1989).

[34] M. Yi, D. H. Lu, R. Yu, S. C. Riggs, J.-H. Chu, B. Lv, Z. K. Liu, M. Lu, Y.-T. Cui, M. Hashimoto, S.-K. Mo, Z. Hussain, C. W. Chu, I. R. Fisher, Q. Si, and Z.-X. Shen, Phys. Rev. Lett. 110, 067003 (2013).

[35] H. Miao, L.-M. Wang, P. Richard, S.-F. Wu, J. Ma, T. Qian, L.-Y. Xing, X.-C. Wang, C.-Q. Jin, C.-P. Chou, Z. Wang, W. Ku, and H. Ding, Phys. Rev. B 89, 220503 (2014).

[36] M. Yi, Z. Liu, Y. Zhang, R. Yu, J. Zhu, J. Lee, R. Moore, F. Schmitt, W. L, S. Riggs, J.-H. Chu, B. Lv, J. Hu, M. Hashimoto, S.-K. Mo, Z. Hussain, Z. Mao, C.-W. Chu, I. Fisher, Q. Si, Z.-X. Shen, and D. Lu, arXiv:1506.03888 [cond-mat.supr-con] (2015).

[37] I. Okada and K. Yosida, Prog. Theor. Phys. , 1483 (1973).

[38] J. von Delft, G. Zaránd, and M. Fabrizio, Phys. Rev. Lett. 81, 196 (1998).

[39] Details differ for $\omega_k \gtrsim T_{\mathrm{K}}^{\mathrm{orb}}$, because the scAHM crossover scales on the left are larger than on the right[40]..

[40] To more clearly reveal the intermediate regime, one could study the Kondo-type model associated with our AHM, derived by [22]. By tuning its bare parameters independently, arbitrarily large ratios of $T_{\mathrm{K}}^{\mathrm{sp}}/T_{\mathrm{K}}^{\mathrm{orb}}$ can be achieved.

[41] K. M. Stadler, A. K. Mitchell, J. von Delft, and A. Weichselbaum, to be published (2015).

[42] G. Moeller, Q. Si, G. Kotliar, M. Rozenberg, and D. S. Fisher, Phys. Rev. Lett. 74, 2082 (1995).

[43] D. S. Fisher, G. Kotliar, and G. Moeller, Phys. Rev. B 52, 17112 (1995).

[44] K. Held, R. Peters, and A. Toschi, Phys. Rev. Lett. 110, 246402 (2013).

[45] F. Verstraete, A. Weichselbaum, U. Schollwöck, J. I. Cirac, and J. von Delft, arXiv:cond-mat/0504305; published as Phys. Rev. B 80, 165117 (2009).

[46] F. B. Anders and A. Schiller, Phys. Rev. Lett. 95, 196801 (2005).

[47] R. Peters, T. Pruschke, and F. B. Anders, Phys. Rev. B 74, 245114 (2006).

[48] R. Žitko and T. Pruschke, Phys. Rev. B 79, 085106 (2009).

[49] R. Žitko, Computer Physics Communications 180, 1271 (2009).

[50] K. Stadler, A. Weichselbaum, and J. von Delft, to be published (2015).

[51] A. Weichselbaum, Phys. Rev. B 84, 125130 (2011).

[52] W. C. Oliveira and L. N. Oliveira, Phys. Rev. B 49, 11986 (1994).

[53] P. Werner, A. Comanac, L. de' Medici, M. Troyer, and A. J. Millis, Phys. Rev. Lett. 97, 076405 (2006).

[54] K. Haule, Phys. Rev. B 75, 155113 (2007).